communications
earth & environment

ARTICLE

https://doi.org/10.1038/s43247-023-00772-y OPEN

Evidence of Arctic methane emissions across the mid-Pleistocene

Giuliana Panieri [1✉], Jochen Knies[1,2], Sunil Vadakkepuliyambatta[3], Amicia L. Lee[4,6] & Carsten J. Schubert [5]

During the Pleistocene, Earth's climate changed dramatically. The mid-Pleistocene transition (MPT; ~1.3–0.7 million years (Ma)) featured an important ice volume increase at both poles. The evolution of large Arctic ice sheets caused the sequestration of methane as free gas and hydrates in subseabed sediments. Ice volume changes, associated with variable pressures and temperatures, perturbed those giant reservoirs, causing methane leakages. Here, we present borehole data from the Arctic–Atlantic gateway region, providing foraminiferal stable carbon isotope and source-specific biomarker evidence that reveals three main seafloor leakage episodes that occurred prior to and across the mid-Pleistocene transition. By combining borehole data with hydrate stability modelling, we propose that tectonic stress changes associated with large ice volume early build-up and wastage during the mid-Pleistocene controlled episodic methane leakages from subsurface reservoirs. Our data indicate methane release, showing a potential scenario for vast Arctic areas storing methane that are now affected by ongoing ice volume decrease.

[1] CAGE – Centre for Arctic Gas Hydrate, Environment and Climate, Department of Geosciences, UiT The Arctic University of Norway, Tromsø, Norway. [2] Geological Survey of Norway, Trondheim, Norway. [3] National Centre for Polar and Ocean Research (NCPOR), Ministry of Earth Sciences, Government of India, Headland Sada, Goa, India. [4] Department of Geosciences, UiT The Arctic University of Norway, Tromsø, Norway. [5] EAWAG, Swiss Federal Institute of Aquatic Science and Technology, Kastanienbaum, Switzerland. [6] Present address: JBA Risk Management, No 1 Broughton Park, Old Ln, Broughton, Skipton BD23 3FD, UK. ✉email: giuliana.panieri@uit.no

Through the Quaternary (from 2.6 Ma years ago to the present), glacial and interglacial cycles driven by orbital processes caused the growth and decay of ice sheets in both hemispheres. These enormous changes in ice volume affected the stability of large amounts of methane stored as free gas and hydrate in the subseabed[1].

One of the most intriguing time intervals of the Quaternary is the mid-Pleistocene transition (MPT) between ~1.3 and ~0.7 Ma[2], when the periodicity of glacial cycles gradually changed from dominantly 41- to 100-kyr cycles, without any known attributable change in orbital forcing[3,4]. The proposed internal climate feedback mechanisms include changes in ocean circulation[5], sea ice extent[6] and ice sheet dynamics[7]. These changes led to modifications in the global carbon cycle because of decreasing atmospheric CO_2 (pCO_2)[8] and accurately reflected the onset of 100-kyr glacial cycles. The exposure of continental formations under ice sheets, after the removal of a thick regolith cover by glacial erosion, enabled the build-up of taller ice sheets during the MPT, favouring the establishment of more extended periods of ice ages[9]. The increase in the severity of glaciations that paralleled the emergence of the 100-kyr cycles at approximately 1250 ka impacted the Antarctic ice volume, which increased abruptly at ~900 ka[7]. In the Northern Hemisphere, ice sheets likely covered a similar area prior to and after the MPT[2,10], implying that post-MPT ice sheets were substantially thicker than pre-MPT glaciation[2]. The Barents and Kara Seas shelves (Fig. 1) are areas predestined for building large ice sheets during glaciation[7]. These Eurasian marine-based grounded ice sheets may have contributed considerably to the 'surplus' glaciations since the MPT[11].

The first shelf-edge glaciations in the Barents Sea occurred between 1.6 and 1.5 Ma, synchronous with a pronounced increase in subglacial erosion[12,13]. Evidence for mega-scale tabular icebergs or ice sheets grounding on the Yermak Plateau and NW Svalbard[14–16] (Fig. 1) suggests an important increase in the ice volume of the Eurasian ice sheets between ~950 and ~800 ka. This time interval falls within the period of a substantial increase in the sea ice extent in the Pacific[6], enhanced deep carbon storage in the Atlantic[17], and Antarctic ice volume increase[7].

While there are consistencies in a substantial bipolar increase in ice volume throughout the MPT, the effect of these 'surplus' glaciations at both poles on the widely occurring methane and gas hydrate reservoirs[18,19] in previously glaciated continental margins remains unknown.

In the Arctic, the most major known methane expulsion events from dissociating gas hydrates occurred during the rapid melting of kilometre-thick ice sheets at the end of the last (~22–18 kyrs BP) and penultimate (~140 kyrs BP) glaciations[20–24]. However, prior to those events, no direct evidence of methane outbursts from decomposing hydrates and underlying gas accumulations in the circum-Arctic exists. The question of whether the 'surplus' glaciations and the evolving thicker ice sheets throughout major transitions in Quaternary climate dynamics had any impact on the stability of Arctic gas hydrates remains unresolved, and it cannot currently be tested due to the paucity of greenhouse gas data from ice core records[25].

To assess whether changing Arctic ice sheet dynamics impacted or had a causal effect on submarine methane emissions during the Quaternary, we combined foraminiferal stable carbon isotope and source-specific biomarker records from Ocean Drilling Program (ODP) Site 912 (Yermak Plateau, NW Svalbard) (Fig. 1 and Supplementary Tables 3 and 4) with numerical modelling of gas hydrate stability (Supplementary Fig. 3). The findings suggest that three major methane seafloor emissions (ME I, ME II, and ME III) occurred parallel to the increased Northern Hemisphere ice volume around the MPT. We promote tectonic stress, as suggested from modelling experiments for the Arctic–Atlantic gateway region[26], as the dominant factor for these seafloor leakages prior to and across the MPT, causing repeated fault reactivation linked to glacial isostatic adjustments (GIAs) due to advancing and retreating ice sheets in the Barents Sea since its first shelf-edge glaciation at ~1.6–1.5 Ma.

Results

Lithostratigraphy and age model. ODP Leg 151, Hole 912A (79°57.557'N, 5°27.360'E, 1037 m water depth), is located on the southern Yermak Plateau (Fig. 1). Hole 912A drilled into a 145.4-m-thick sequence of predominantly dark grey, unlithified,

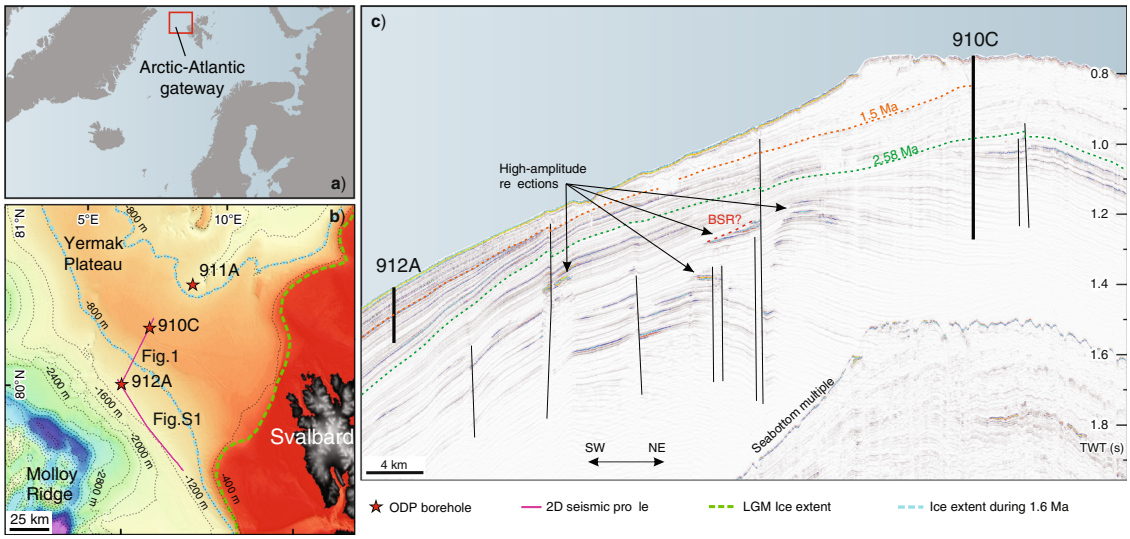

Fig. 1 ODP Leg 151 boreholes location and seismic data. a Map showing the Arctic–Atlantic gateway where the Yermak Plateau was drilled during ODP Leg 151 and the study area (red rectangle). **b** Bathymetry of the Yermak Plateau showing ODP Leg 151 boreholes and the location of the seismic profile (**c**) used in this study crossing two holes: Hole 912A and Hole 910C. The ice extent during the Last Glacial Maximum (LGM)[91] and 1.6 Ma (assumed based on ref. [92]) are shown in the figure with green and light blue dotted lines, respectively. **c** The seismic data show the BSRs and gas-charged sediments visible as high-amplitude reflections. Age markers 1.5 (orange dotted line) and 2.58 Ma (green dotted line) are adopted from previous studies[29]. Fig. S1 refers to Supplementary Fig. 1.

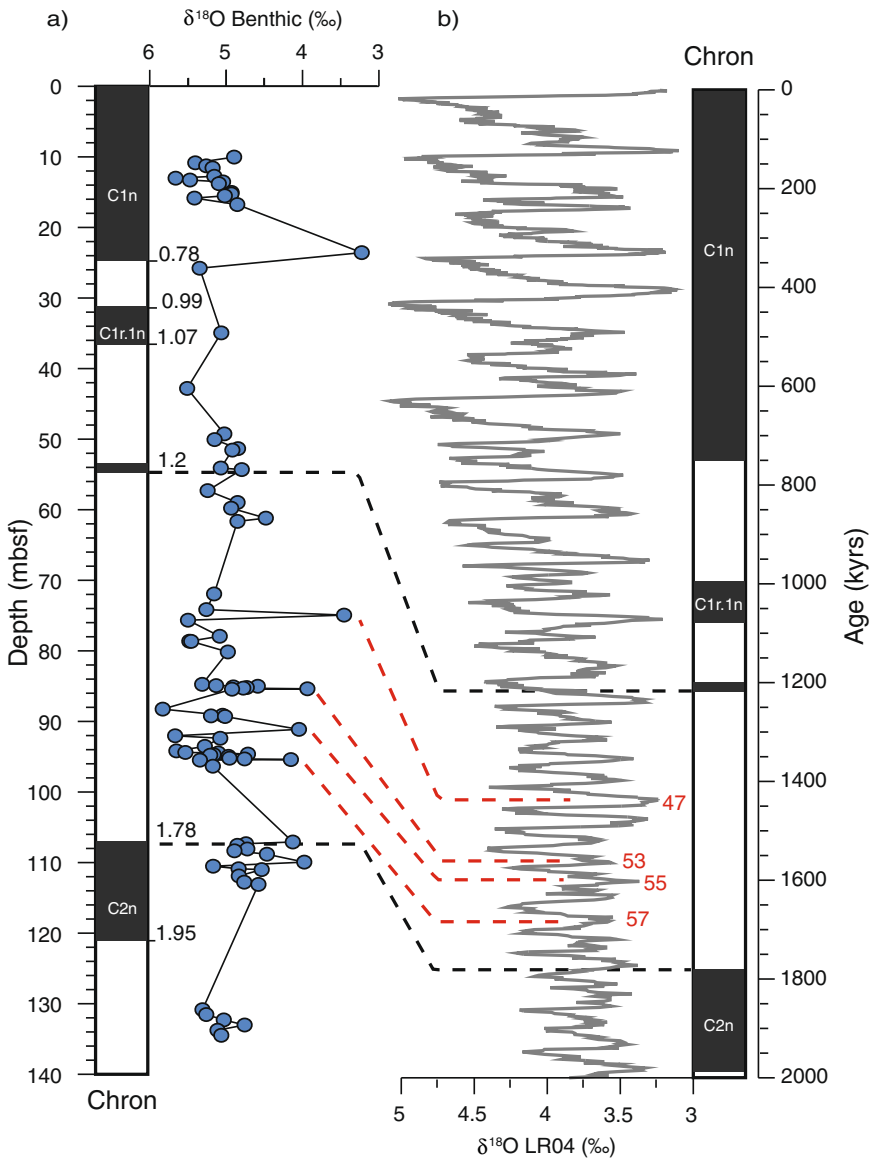

Fig. 2 Stratigraphic correlation of ODP Hole 912A with global records. a Palaeomagnetic interpretation[27] and new benthic stable oxygen isotope data in Hole 912A vs depth (metre below seafloor, mbsf). Ages for chron boundaries are according to ref. [93]. **b** Global LR04 stable oxygen isotope stack[30] and palaeomagnetic chrons vs age. Black stippled lines indicate magnetic chron boundaries between ~1.2 and ~1.8 Ma. Based on linear sedimentation rates between chron boundaries, interglacial marine isotope stages (MISs) 47, 53, 55, and 57 are identified by visual correlation of light stable oxygen isotope intervals (red stippled lines).

structureless to moderately bioturbated silty clays and clayey silts[27,28]. The entire sedimentary section represents the last ca 2.2 Ma[29].

The age model is based on magneto- and biostratigraphic data[27] and is supported by new stable oxygen isotope analyses of benthic foraminifera, *Cassidulina teretis-neoteretis*, from this study (Fig. 2 and Supplementary Tables 2 and 3) and high-resolution seismic data that permit correlation between ODP Holes 910C, 911A, and 912A[29] (see details in the Method section). Briefly, the interval from 24.6 to 36.5 metre below the seafloor (mbsf) is characterised by variable inclinations corresponding to the upper Matuyama Chron (~0.78–0.99 Ma) and the Jaramillo Subchron (C1r.1n, ~0.99–1.07 Ma). The Cobb Mountain (C1r.2r-1n; 1.20–1.21 Ma) and Olduvai Subchrons (C2n, ~1.78–1.95 Ma) are identified within 53.8–54.7 and 107.1–121.6 mbsf, respectively. Sedimentation rates between these magnetic boundaries vary between 4 and 13 cm/ka (see details in the Method section). Correlating the benthic $\delta^{18}O$ record of Hole 912A to the global LR04 stack[30] (Fig. 2) helps to further constrain the stratigraphic framework for the onset of the MPT. Several intervals with lighter $\delta^{18}O$ values (<4‰) between 75 and 95 mbsf are correlated to interglacial marine isotope stages (MIS) 47–57 (~1.4–1.6 Ma). Applying this age model, the occurrence of ice-rafted debris (IRD) input (>500–1000 µm; Supplementary Table 6) and the number of dropstones (Supplementary Table 7) show initial peaks at ~1.6–1.5 Ma and a subsequent gradual increase across the MPT to an IRD maximum at approximately 1 Ma (Supplementary Fig. 2). Adjacent to Site 912, high-resolution seismic data show high-amplitude reflections, suggesting a potential gas accumulation[29] (Fig. 1 and Supplementary Fig. 1). Some of these bright reflections show characteristics of a bottom-simulating reflection (BSR), indicating the presence of gas hydrates[31]. In addition, numerous faults are associated with gas accumulations, indicating faults as potential migration pathways

for fluids in this area. BSRs also occur south of Site 912, along with multiple bright high-amplitude reflectors and faults (Fig. 1 and Supplementary Fig. 1).

Microscopic and spectroscopic analyses of benthic foraminiferal tests. Well-preserved pristine foraminiferal tests in sediments from Hole 912A are optically smooth and have high reflectance and transparency, except during intervals prior to and across the MPT, in which the tests have experienced different degrees of diagenetic alteration. In these intervals, the foraminiferal tests appear white or yellow in reflected light microscopy and have lost their optically smooth surface texture, transparency, and reflectance. Often, the tests are characterised by a coating of a secondary phase confirmed by scanning electron microscope (SEM) observations. Further analyses with energy-dispersive X-ray spectroscopy (EDS) and electron backscattered diffraction on tests of *Melonis barleeanus*, *Fursenkoina* cf. *acuta*, *Stainforthis feyilingi* and *Cassidulina* spp. reveal that the coating is a secondary authigenic carbonate overgrowth. The authigenic carbonate coating is at least 10-μm thick and is present both on the test walls of the outer chambers and on the test walls of the inner chambers. Carbonate precipitation embedded minute grains of siliceous and aluminium mineral phases (Fig. 3). Some of the foraminiferal tests contain framboidal pyrite (Fig. 3). Because the foraminiferal biogenic calcite and authigenic calcite layer phases have the same crystallographic orientation, foraminifera serve as preferred nucleation templates for authigenic calcite precipitation at methane seeps[32].

Stable isotopic data of foraminiferal species. A composite stable carbon ($\delta^{13}C$) record was constructed from various planktonic (*Neogloboquadrina pachyderma*) and benthic foraminiferal species (*Cassidulina teretis-neoteretis, Melonis barleeanus, Fursenkoina* cf. *acuta and Stainforthia feylingi*) (Fig. 4; Supplementary Table 3 displays all the $\delta^{13}C$ results also from foraminifera values that are not shown in the composite record). The $\delta^{13}C$ values of planktonic and benthic foraminifera range between −1.2 and 0.1‰ and between −2.0 and 0.5‰, respectively, in almost all sediment horizons of Hole 912A and are consistent with values characteristic of well-oxygenated marine conditions from the Arctic Ocean and northern Barents Sea[33]. However, prior to and across the MPT, both planktonic and benthic foraminifera show major negative carbon isotope excursions at three intervals: between 1.66 and 1.57 Ma (ME I), where the values range from −0.78‰ in *C. teretis-neoteretis* to −23.2‰ in *F.* cf. *acuta*, between 1.26 and 1.04 Ma (ME II), where −1.06‰ is the value recorded by *C. teretis-neoteretis* and −28.91‰ is the lowest recorded by *F.* cf. *acuta* and between 0.81 and 0.72 Ma (ME III), where the values range between −3.24 and −12.91‰ in planktonic foraminifera *N. pachyderma* (Fig. 4 and Supplementary Table 3). Those negative values recorded in benthic and planktonic foraminifera are consistent only with a foraminiferal signal affected by secondary carbonate overgrowth. Similar depletion of the carbon isotopic composition was previously reported from ancient methane seeps[34].

Biomarkers. Anaerobic oxidation of methane (AOM)-related biomarkers of archaea (archaeol) and sulfate-reducing bacteria (SRB) (iso- and anteiso-$C_{15:0}$ fatty acids) were identified in all the samples analysed within the three foraminiferal carbon isotope excursions recorded prior to and across the MPT. The average concentrations of archaeol, iso-$C_{15:0}$ and anteiso-$C_{15:0}$ for bacterial lipids were slightly higher at ME III at ~1.64 Ma (0.14, 1.02, and 1.76 $\mu g\,g^{-1}$ sediment) than at ME II and ME I in the MPT (0.33, 0.72, and 1.29 μg/g sediment) (Fig. 4 and Supplementary Table 3). The highest concentrations of bacterial lipids, here iso- and anteiso-branched C15:0 fatty acids prior to and across the MPT (~1.67 and 2.85 $\mu g\,g^{-1}$ dry weight, respectively), indicate the presence of SRB[35], which have been found in AOM environments (ref. [36] and references therein). We suggest that SRB are the species occurring in our core, although other bacteria could comprise the fatty acids. However, sulfate reduction performed by SRB is the overwhelming process for organic matter degradation in the marine realm[37]. The presence of AOM-related biomarkers of archaea (archaeol) and SRB exactly where the three foraminiferal carbon isotope excursions occur suggests methane oxidation in the sediment and involvement of methane-oxidising microorganisms in the precipitation of secondary carbonate on foraminiferal tests.

Discussion

Evidence for Arctic methane emissions across the mid-Pleistocene. Geochemical and stratigraphic data from Site 912 on the Yermak Plateau provide evidence for episodic methane release prior to and across the MPT. Migration of methane was activated three times: from ~1.6 to 1.5 Ma, during the tipping point of the first Barents Sea shelf-edge glaciation and across the MPT, at the onset at ~1.2 and at the end of the midpoint at ~0.7 Ma, coinciding with an important increase in the ice volume of the Eurasian ice sheets. The three inferred main seafloor methane emission episodes are labelled as ME I, ME II and ME III (Figs. 4 and 5). The source of methane is believed to be derived from deep sediments, corresponding to old carbon reservoirs[38]. Recent modelling results in the study region revealed that gaseous hydrocarbons, originating from Miocene-aged terrestrial organic matter, accumulated in early Pleistocene sedimentary sequences and have been episodically released at the seafloor since ~1.5 Ma[26]. Our seismic data at Site 912 support a deep methane source, showing a vertical fluid migration system transporting fossil hydrocarbons from greater depths (Fig. 1 and Supplementary Fig. 1).

When methane reaches the seafloor, biogeochemical processes that involve microbes, chemical elements, and minerals leave their fingerprint in the sedimentary archive. At ME I, ME II, and ME III, we recognise secondary overgrowth on foraminiferal tests with isotopically light carbonate that resulted from methane oxidation together with the presence of pyrite around and inside foraminiferal tests (Fig. 3). These observations suggest synsedimentary methane oxidation at the sulfate–methane transition zone (SMTZ) close to the seafloor or within the first decimetres. That this methane was oxidised at the seafloor or in subsurface sediments is further indicated by the negative $\delta^{13}C$ excursions recorded in foraminifera (up to −28.9‰). Depleted $\delta^{13}C$ isotope values in foraminifera are widely considered to reflect methane seepage. They are used to identify the periodic release of methane at various times in Earth's history[24,39–42]. Foraminifera can incorporate ^{13}C-depleted methane-derived dissolved inorganic carbon (DIC) during biomineralization while alive[43,44] and may ingest ^{13}C-depleted methanotrophic microbes[43,44]. Recent evidence of foraminifera inhabiting sediments impacted by gas hydrate dissociation shows a close association with putative methanotrophs[45]. However, the shift to more negative $\delta^{13}C$ values at Site 912 prior to and across the MPT (up to −28.9‰) is the result of secondary authigenic carbonate overgrowth at the SMTZ, as indicated by the microscopic inspection and EDS and EBDS analyses (see Methods and data displayed in Fig. 3). The formation of authigenic carbonates by precipitation of bicarbonate with calcium ions follows an increase in alkalinity due to two relevant biogeochemical processes: (1) the oxidation of organic matter under anoxic conditions or (2) the AOM[46]. The first process would release DIC, with isotopic composition of the organic material that settles to the seafloor, which at the water

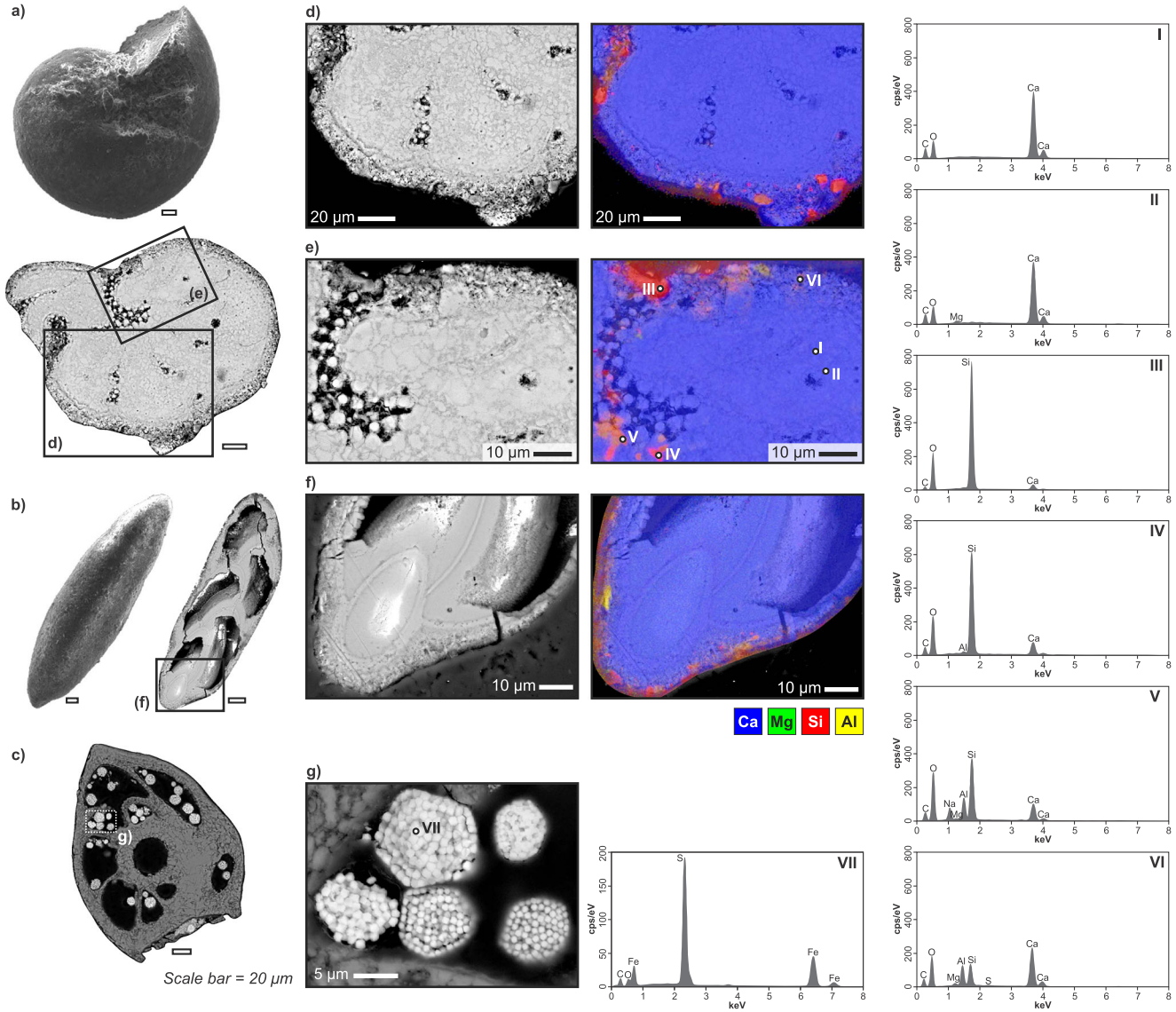

Fig. 3 Examples of diagenetic alterations in foraminiferal tests from methane sites. The images are from specimens from ME I, where the sediments were affected by past methane emissions and exhibit test alteration evidenced by backscatter-scanning electron microscopy (SEM) images (**a**, **b**) and energy-dispersive X-ray spectroscopy (EDS) images (**c**–**g**). SEM images and backscatter electron (BSE) images from cross-sections of the benthic foraminifera *Melonis barleeanus* (**a**) and *Fursenkoina* cf. *acuta* (**b**) exhibit the presence of methane-derived authigenic carbonate (MDAC) coatings around the calcite test. In *M. barleeanus* (**a**), the primary test with evident pores is still visible on the upper left side of the image corresponding to the first chambers. *Fursenkoina* cf. *acuta* (**b**) tests have lost the optically smooth surface texture, transparency and reflectance. They are pervaded by a pervasive coating of MDAC, presenting moderate diagenetic alteration, according to ref. [94]. The BSE images of cross-sections of *M. barleeanus* (**d**, **e**) and *Fursenkoina* cf. *acuta* (**f**) show the presence of the MDAC coating throughout the tests. The secondary electron images show the chemical characterisation of foraminifera primary tests and secondary overgrowth, presented as point analyses (I–VI in panel **d**, with relative spectra) and as compositional maps (blue indicates calcium, Ca; green indicates magnesium, Mg; red indicates silicon, Si; yellow indicates aluminium, Al). SEM image and backscatter electron (BSE) images from cross-sections of the benthic foraminifera *Cassidulina teretis* (**c**–**g**) show the presence of rounded clots formed by micrometric pyrite crystals precipitated inside the test (point analyses VII in panel **g** and relative spectra).

depth of Site 912 was mainly phytoplankton and marine algae with an isotopic value of approximately −21‰[47]. Hence, as observed in our data, this process would never result in isotopically depleted foraminiferal shells (up to −28.9‰). On the other hand, the second process would release very isotopically depleted DIC since oxidised methane would result in the formation of DIC that is isotopically very light, for example, down to −46‰ in cores from the north-eastern South China Sea[48]. It must also be noted that at the current SMTZ in Hole 912A, at ca. 15 mbsf[27], the $\delta^{13}C$ values of foraminifera are within the range of the normal marine environment (~−0.5‰).

Interestingly, the $\delta^{13}C$ values of *F.* cf. *acuta* and *S. feylingi* are always more negative than those recorded by *C. teretis-neoteretis* (Fig. 4). While *C. teretis-neoteretis* are epifaunal-shallow species[49,50], *Fursenkoina acuta* and *S. feylingi* are deep infaunal species[51] that exhibit a lower $\delta^{13}C$ in the primary shell[52,53]. This phenomenon occurs because the isotopic composition of the bottom water controls the isotopic composition of epifaunal species. In contrast, the infaunal species is controlled by the pore-water isotopic composition, where the DIC values already include DIC derived from the degradation of isotopically light organic material. Hence, the ^{13}C-depleted values of the diagenetic

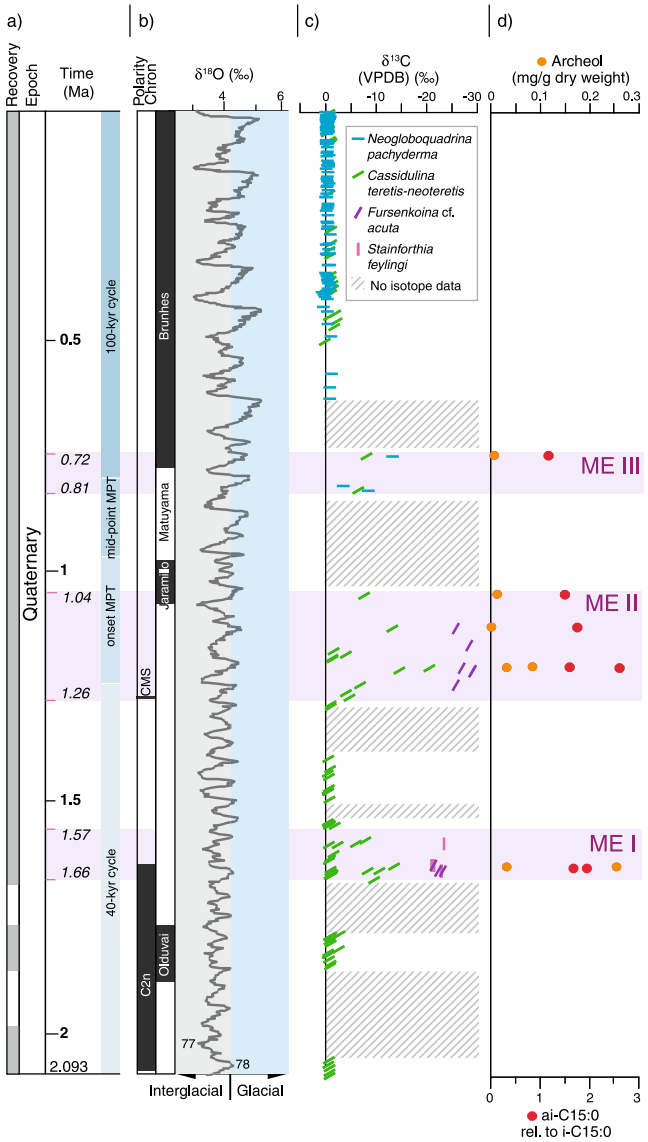

Fig. 4 Compilation of background data and biogeochemical evidence indicate methane leakages during methane excursions ME I–ME III in Hole 912A. a The recovered sediment from Hole 912A is shown in grey. Epochs and ages are according to ref. [29]. The palaeomagnetic record is from ref. [27], where black = normal polarity and white = reversed polarity. **b** Benthic $\delta^{18}O$ record LR04 stack (in ‰ vs Vienna PeeDee Belemnite VPDB)[30]. **c** $\delta^{13}C$ stable isotopes of selected planktonic and benthic foraminifera expressed in ‰ vs VPDB. Depleted values characterise methane emission events ME I, ME II and ME III. **d** AOM lipid biomarkers measured within ME I, ME II and ME III show the presence of anaerobic oxidation of methane (AOM)-related biomarkers of archaea (archaeol) and sulfate-reducing bacteria (SRB). The typical AOM consortia indicate the presence of methane oxidation and processes involved in the formation of secondary authigenic carbonate overgrowth in foraminiferal tests. See Supplementary Table 3 for the complete dataset of $\delta^{13}C$ values measured in planktonic and benthic foraminifera and Supplementary Table 4 for the biomarker data.

carbonate overgrowth on *F.* cf. *acuta* and *S. feylingi* shells occur because the isotopically light carbonate from AOM is added to the already negative values of the primary tests biomineralised in an infaunal habitat. The presence of pyrite inside the foraminiferal tests (Fig. 3), pyrite-encrusted tube-like features that are probably fossil worm tubes, and the increase in total sulfur (Supplementary Fig. 2) at ME I, ME II and ME III corroborate the syn-sedimentary nature of the methane emissions. It supports observations of similar encrusted tubes found in cold seeps at Vestnesa Ridge that are attributed to frenulate siboglinid worms[54,55], typical seep fauna.

Other biological evidence for a syn-sedimentary nature of the methane leakages at the three past methane excursions involves microbial biomarkers. According to former publications[56,57], methane oxidation was related to a consortium of bacteria and archaea[58], namely, the AOM community. However, according to recent studies[59,60], methane oxidation was also associated with Archaea that do not build consortia. In our research, we found lipid biomarkers of Archaea but also SRB in the sediments prior to and across the MPT (Fig. 4 and Supplementary Table 4). Furthermore, the strongly ^{13}C-depleted values of the archaea-derived compounds (archaeol and OH-archaeol) provide compelling evidence for AOM. The distinct negative ^{13}C-depleted value of archaeal lipids of −93.7‰ at 1.6 Ma and −66.3‰ at the MPT reflect the utilisation of methane as a carbon source, as indicated by several previous investigations[61–64]. Values of archaeol $\delta^{13}C$ (−62‰) similar to those measured at the MPT were obtained, for example, from microbial mats in 0–2 cm of sediment at the Håkon Mosby Mud Volcano active methane seep site[64,65] and from microbial mats elsewhere (−88‰)[66]. The co-occurrence of the archaeal lipid archaeol, sn-2-hydroxyarchaeol, together with fatty acid-derived SRB is similar to microbial biomarker assemblages found in seepage sites on continental margins[56,67,68].

The archaeal and SRB biomarker concentrations typically reach maxima close to the SMTZ, where archaeal biomarkers are depleted in $\delta^{13}C$[67]. However, the SRB fatty acids in our sediments are not heavily isotopically depleted (isoC15:0, $\delta^{13}C = -25.3$‰; anteiso C15:0, $\delta^{13}C = -26.3$‰), which means that they are not involved in AOM but rather only in organic matter degradation. As mentioned above, it is not unusual that AOM is performed only by archaeal cells (namely, ANME-2). Hence, it is very likely that a single organism performed AOM in our core. Altogether, we can state that in addition to the isotopic composition of the carbonaceous overgrowth of the foraminifera, we find strong evidence for AOM close to the surface sediments by the drastically depleted isotopic composition of biomarkers related to methane-oxidising microorganisms.

Mechanisms for methane leakage. The high-amplitude reflections and BSRs adjacent to Site 912 suggest the presence of shallow gas accumulations rising from deep reservoirs below the Yermak Plateau (Figs. 1 and 5). The BSRs occur adjacent to faults and fractures, which likely supply gas to the current hydrate stability zone. These faults may also have acted as conduits for transferring old carbon to the seafloor during past methane emission episodes ME I, ME II and ME III, as postulated and modelled for Vestnesa Ridge, NW Svalbard[26,69].

Past dynamics of Arctic methane seepage are generally inferred to be associated with the repeated waxing and waning of glacial ice[20,21,34]. On the formerly glaciated Barents Sea continental margins, high-pressure and low-temperature subglacial conditions have favoured the sequestration of methane and heavier natural gases in hydrate form[70]. It is known that such hydrates experienced dissociation after the Last Glacial Maximum (LGM) when the ice sheet started to retreat[20,21,71]. The consequent large-scale methane release resulted in the formation of seafloor craters and domes[20,21] and precipitation of MDAC[22]. Similar large craters have been recently found in the frozen Yamal Peninsula in Siberia[72,73]. Researchers have suggested that increased temperature causes permafrost thawing and collapse for these remarkable features, releasing methane trapped as a hydrate in the frozen ground[73].

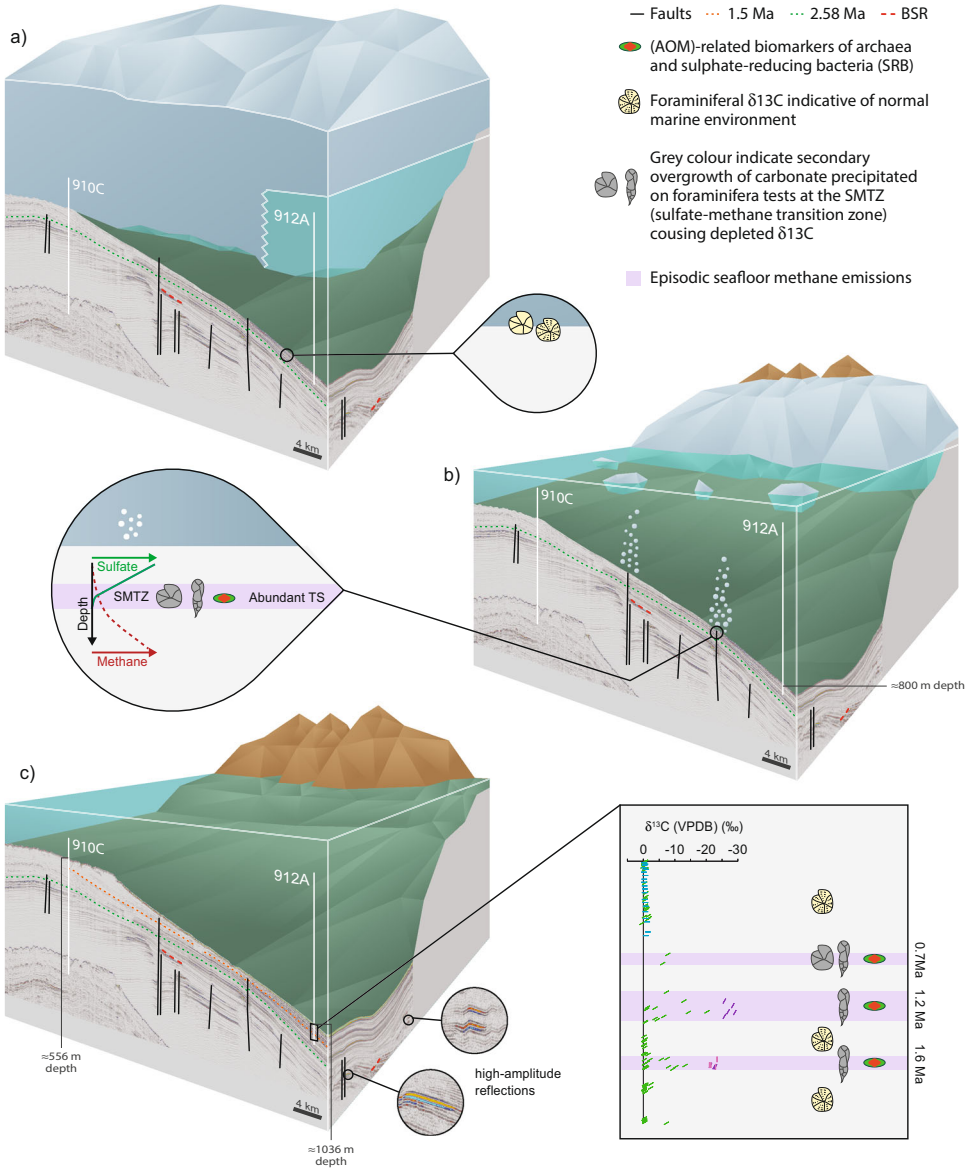

Fig. 5 Mid-Pleistocene methane release on the Yermak Plateau, NW Svalbard. a Conceptual model of glacial intensification (~1.6–1.5 Ma) and MPT ice sheet grounding (~1.0 to ~0.8 Ma). The locations of ODP Sites 910 and 912 are indicated. **b** Upon glacier retreat, hydrate dissociation and fault reactivation contributed to intense methane release at the seafloor during ME I, ME II and ME III. **c** Present-day environment in the study area, where the stable isotope compositions ($\delta^{13}C$) of foraminifera and biomarker analysis from ODP Hole 912A sediments indicate evidence of past methane release (not to scale). High-amplitude reflections in seismic data indicate methane in the sediments below the Gas Hydrate Stability Zone (GHSZS).

However, in deep-water settings (>1000 m), such as the Yermak Plateau, gas hydrates trapped in sediments are less vulnerable to temperature variations. Instead, pressure changes due to sedimentation or erosion can considerably affect hydrate stability (e.g., ref. [74]). Fault reactivation and syn-depositional deformation due to changes in ice sheet configuration cause glacial tectonic stress, inducing rapid build-up of excess pore fluid pressure and the subsequent flow of fluids through faults and triggering fault movement and fracturing[69,75,76]. In a deep-water (>1000 m) gas hydrate system on Vestnesa Ridge (off NW Svalbard), repeated tapping of hydrocarbon reservoirs due to fracture formation and reactivation promoted by GIA and forebulge formation has been responsible for the long-term pattern of methane seepage[23,24,26,34,77].

To test the impact of gas hydrate evolution on methane seepage, the gas hydrate stability zone (GHSZ) at Site 912 was simulated between 0.7 and 2.0 Ma, incorporating transient variations in sea level[78] and varying sedimentation rates[29]. The model shows that the base of the GHSZ shifted multiple times during the modelled period in response to changes in sea level and increasing overburden due to sedimentation and deposition of IRD-rich deposits at the study site (Supplementary Fig. 3). Most of these shifts at the base of the GHSZ were <20 m. Such variations might have resulted in increased pore pressure at the base of the GHSZ and methane release at the seafloor (e.g., ref. [74]). However, since carbon isotope anomalies in planktonic and benthic foraminifera and AOM biomarker abundance occur only prior to and across the MPT at Site 912, we rule out the possibility of large-scale methane emissions controlled by sea-level-induced variability in the GHSZ. Alternatively, we propose that shelf-edge glaciations and associated reactivation of faults and fractures trigger methane release at the seafloor during episodes ME I, ME II and ME III. The onset of episodic seafloor seepage during ME I is associated with the end of a phase

characterised by high sediment input to the trough mouth fan systems offshore Svalbard, suggesting strong glacial erosion and the development of large ice sheets over Svalbard[13], also testified by an increase in IRD and dropstones in Hole 912A (Supplementary Fig. 2). On the Yermak Plateau, this glacial intensification is best illustrated by the start of crestal erosion and the first occurrences of large iceberg plough marks on the eastern and western slopes[29]. Recent modelling results from a broader study region (W Svalbard and the Yermak Plateau) indicate that glacial forebulge formation during extensive ice growth and decay in the same period caused extensional fracturing, resulting in fault damage of potential gas accumulations underlying the vast study area[26]. A similar mechanism has been proposed for methane seepage at Vestnesa Ridge, which hosts a gas hydrate system >50 km seaward from the ice sheet grounding line and 100 km seaward of the maximum ice extent during the LGM[79], and during the penultimate glacial maximum (~160,000–133,000 years ago), when the ice sheet fluctuation resulted in a vertical lithosphere displacement of up to approximately 60 m[23]. Hence, glacially driven forebulge formation is extensive, and ice wastage during numerous Pleistocene glacial–interglacial cycles has potentially caused large-scale methane release upon deglaciation due to fracture formation and fault reactivation.

Mid-Pleistocene methane emissions during intervals of Arctic ice sheet growth and wastage. We provide evidence of Arctic methane seepage dynamics paralleled by expansive mid-Pleistocene ice sheets in the wider Barents Sea region. Our empirical observations of enhanced methane seepage during episodes ME I–ME III support recent modelling results proposing repeated forebulge uplift and subsidence during glacial cycles with associated fracture formation and reactivation since the first shelf-edge glaciation of the Barents Sea ice sheet[26,80]. However, our observations further indicate that with increased ice volumes and recurrent glacial–interglacial cycles during the mid-Pleistocene, reservoirs of old carbon (e.g., gas hydrates and shallow gas accumulations) were repeatedly affected by fault damage, leading to persistent migration pathways and thus widespread methane seepage. Considering the prevalence of old carbon reservoirs beneath glaciated continental margins across the circum-Arctic, an area of 33 million km^2 of hydrocarbon reserves, and the fact that grounded ice sheets directly influenced this region during the LGM and previous glaciations[20,81], glacially driven forebulge formation and ice wastage during Pleistocene glacial–interglacial cycles potentially caused large-scale methane release upon deglaciation. Indeed, remnants of methane leakage on formerly glaciated margins since the last deglaciation are widespread in the circum-Arctic[73,82,83]. Whether leaking gas from old carbon sources contributed to an enhanced atmospheric methane concentration once the first shelf-edge ice collapsed ~1.5 Ma years ago remains unresolved. While Greenland ice cores are still underexplored, methane from old carbon sources has been absent in Antarctic ice cores since the last deglaciation[84]. Most of the methane in these ice cores is inferred to be derived from the decomposition of recently formed organic carbon, such as plants and soil. Given the substantial size of old carbon reservoirs in the Arctic[81] and widespread leakage following the last deglaciation[20,22] until today[71,82,83], the apparent small effect of this source on global climate fluctuations remains a mystery.

Methods

Samples for this study were taken at the Bremen IODP repository during three sampling parties. Core depth in centimetres (with zero at the top of the section) is reported throughout.

Chronology. The age model of Hole 912A is originally based on magnetostratigraphic interpretation[27] and subsequently used to establish a comprehensive stratigraphic framework for the Yermak Plateau through integration with paleomagnetic and biostratigraphic interpretation from ODP Hole 910C and Hole 911A as well as the correlation of high-resolution seismic data between all sites[29]. Five age fixpoints were identified in Hole 912A and are illustrated in Fig. 2 and Supplementary Table 1. The interval from 24.6 to 36.5 mbsf is characterised by variable inclinations corresponding to the upper Matuyama Chron (~0.78–0.99 Ma) and the Jaramillo Subchron (C1r.1n, ~0.99–1.07 Ma). The Cobb Mountain (C1r.2r-1n; 1.20–1.21 Ma) and Olduvai Subchrons (C2n, ~1.78–1.95 Ma) are identified between 53.8 and 54.7 and 107.1 and 121.6 mbsf, respectively. Sedimentation rates between these magnetic boundaries vary between 3 and 13 cm kyr^{-1}. Linear sedimentation rates calculated for the three lowermost Subchron boundaries (Cobb Mountain top, Olduvai top and base) in Hole 912A, however, show constant values between 8.7 and 9.2 cm kyr^{-1}. Interpolation of these constant rates provides an age for the onset of methane emission episode (ME) 1 at ~1.67 Ma at ~97 mbsf. The age is further supported by new, though, typically for Arctic sediments, erratic stable oxygen isotope ($\delta^{18}O$) analyses of benthic foraminifera *Cassidulina teretis-neoteretis* (Fig. 2). Applying the same constant sedimentation rate model to the benthic $\delta^{18}O$ record, interglacial MIS 47, 53, 55, and 57 (~1.42–1.64 Ma) are identified by visual correlation of light stable oxygen isotope intervals to the global LR04 stack[30] (Fig. 2). The identification of the MPT (~1.3–0.7 Ma) is approximately constrained by the Brunhes/Matuyama boundary (~0.78 Ma) at 24.6 mbsf and the top of the Subchron Cobb Mountain (~1.2 Ma) at 53.8 mbsf where there are the two methane emission episodes named ME II and ME III respectively. The onset of the second methane emission episode (ME II) coincides with the top of the Cobb Mountain Subchron (~1.2 Ma) and the onset of the third methane emissions ME III coincides with C1n.

Total sulfur and ice-rafted debris count. Sediment samples from Hole 912A were freeze-dried, ground, and homogenised at the Geological Survey of Norway (NGU). Samples for total sulfur contents (30–40 g) were combusted at 1350 °C and analysed using a LECO SC-632. All results are given in weight per cent (wt%) (Supplementary Table 5), and the standard deviation was ± 0.06 wt%. The limits of detection were 0.06 and 0.1 wt%. The IRD count was performed on the free-dried samples; the coarse fraction (500–1000 µm) was determined by wet-sieving and presented as percentages (%) of the bulk fraction (Supplementary Table 6).

Stable isotopic analyses of foraminifera. Benthic (*C.teretis-neoteretis* [Seidenkrantz, 1995], *C.reniforme* Nørvang 1945, *Melonis barleeanus* [Williamson, 1858], *Fursenkoina acuta* [d´Orbigny, 1846], and *Stainforthia feylingi* [Knudsen and Seidenkrantz, 1994]) and planktic foraminifera (*Neogloboquadrina pachyderma sinistral* (sin) [Ehrenberg, 1861] *N. Atlantica* [Berggren, 1972) were picked for isotope measurements from the dry residue of the >125-µm size fraction. These species were selected since they are abundant throughout the cores, and some of them (*C.teretis-neoteretis, Melonis barleeanus*, and *Neogloboquadrina pachyderma sinistral*) are common in the Arctic Ocean[33,85,86] and have already been investigated at Arctic seep sites[32,34,86,87]. Each sample of *C. teretis-neoteretis* (142 samples), *M. barleeanus* (27 samples), *F. cf. acuta* (10 samples), *S. feylingi* (4 samples), and *N. pachyderma* sin (110 samples) consisted of 10–20 tests. Foraminiferal shells were placed in 4.5 mL vials and flushed with He gas. Five drops of water-free H_3PO_4 were added manually. After equilibration (>3 h at 50 °C), the samples were analysed. Carbon ($\delta^{13}C$) and oxygen ($\delta^{18}O$) isotope analyses of foraminiferal tests were performed using a Thermo Scientific MAT253 IRMS coupled to a Gasbench II at UiT. In-house standards (1.96‰, −10.21‰, and −48.95‰ for ($\delta^{13}C$ and −2.15‰ and −18.59‰ for ($\delta^{18}O$) were used for calibration and analytical precision was estimated to be better than ±0.08‰ for oxygen and ±0.03‰ by measuring the certified standard NBS-19. We report all isotope results in standard delta notation relative to VPDB.

Elemental composition of foraminifera tests. SEM energy-dispersive X-ray analyses of randomly picked individuals of several specimens of *Cassidulina* spp., *Melonis barleeanus*, and *Fursenkoina* cf. *acuta* (>125 µm) from sediment samples from the Hole 912A ME I (sample at 94.49 mbsf) were carried out with a Zeiss Merlin VP Compact SEM equipped with an EDS x-max 80 system by Oxford Instruments, combined with the analytical software AZtec. For 3D analyses, samples were mounted on carbon tape. For 2D sections, samples were mounted in resin blocks and polished with ¼ µm diamond paste and colloidal silica. The samples were carbon-coated with a 5-nm carbon coat to prevent charging. Analyses were performed at an accelerating voltage of 20 kV and a working distance of 9–10 mm with a 120-µm aperture. These EDS data for chemical characterisation are presented as a compositional map in Fig. 3. Normalised element maps are coloured by individual elements and overlain to show chemical variations.

Biomarkers. Biomarker analyses were performed on seven samples chosen where benthic foraminifera exhibited a change in species in the assemblages, and isotopic measurements showed negative carbon excursions. Freeze-dried sediment (20–50 g; Supplementary Table 4) was extracted and homogenised. Total lipids were extracted by a SOLVpro Microwave Reaction System (Anton Paar, Graz,

Austria) at 70 °C for 7 min with 15 mL (7:3; v/v) of dichloromethane (DCM)/methanol (MeOH). For quantification, a known mixture of 5α-cholestane, C19 n-alcohol and C19:0 fatty acid was added to the extract. Total lipid extracts (TLE) were then transferred to separation funnels containing 20 mL of nanopure water (H_2O) with 5% sodium chloride to remove salts. The TLE was recovered from the saline aqueous phase by liquid-liquid extraction using 3 × 10 mL DCM. The extract was run over a Cu column to remove elemental S and over a column filled with Na_2SO_4 to remove traces of water. Extracts were then saponified at 80 °C for 3 h using 3 mL of 1 N KOH in MeOH. After saponification, solvent-extracted nanopure H_2O was added to the saponified TLE. Neutral lipids were recovered by liquid-liquid extraction of hexane, while the acid fraction was extracted from the aqueous phase after the addition of 6 M HCl. Neutrals were further separated using 500 mg/6 mL Isolute Si gel columns (Biotage, Uppsala, Sweden) with increasingly polar solvents. The polar fraction was derivatised (1 h at 80 °C) with N,O-bis-trimethylsilyltrifluoroacetamide (BSTFA, Supelco). Fatty acids were derivatised with 14% BF3/MeOH (Sigma-Aldrich) to produce methyl esters (FAMEs). Archaeol and fatty acids were identified by gas chromatography-mass spectrometry (GC-MS-QP2010 Ultra, Shimadzu) and quantified with a GC2010 gas chromatograph by splitless injection at 280 °C. A Gl Sciences Inertcap 5MS (30 m × 0.25 mm × 0.25 μm) GC column was used. The temperature programme of the oven was held for 1 min at 80 °C, heated to 130 °C at 20 °C/min, and then to 320 °C at 5 °C min^{-1} (held for 10 min). Compound-specific $\delta^{13}C$ values were obtained using gas chromatography isotope ratio mass spectrometry (GC-IRMS). Samples were injected with a TriPlusRSH autosampler into a split/splitless injector operated in splitless mode at 280 °C on a GC-1310 gas chromatograph (Thermo Scientific, Bremen, Germany) equipped with an InertCap 5MS column (30 m × 0.25 mm × 0.25 μm) (GL Sciences, Japan, run with the same temperature profile as above) and interfaced with a Delta V Advantage IRMS (Thermo Scientific) with a ConFlow IV (Thermo Scientific). Isotope values were measured using Thermo Isodat 3.0 software relative to pulses of working gas measured at the beginning and end of each analysis. Sample $\delta^{13}C$ values were normalised to the VPDB scale using known values of isotopic standards (n-C17, 19, 21, 23, 25, 28, and 34 alkanes, Arndt Schimmelmann, Indiana University), which were run at the beginning and end of each sequence, as well as after every 6–8 sample injections.

Transient modelling of gas hydrate stability. The evolution of gas hydrate stability at ODP Site 912 during the period 0.7–2 Ma was simulated by incorporating pressure changes due to sea level variations (from ref. [78]) and pressure and temperature variations due to sedimentation (with sedimentation rates from ref. [29]). The effect of ice load was not accounted for in the model since there is no evidence of grounded glaciers at Site 912. The subsurface temperature evolution was assumed to be gradual, whereas the subsurface pressure change was considered instantaneous. Although multiple glaciations have affected the continental shelf close to Site 912, this model assumes that subglacial conditions did not exist at Site 912 and that the impact of glaciations was negligible. To estimate the variation in the GHSZ at Site 912, a 1D model with 5000 cells (1 m resolution) is generated with the upper boundary at the seafloor and the basal boundary 5000 mbsf. The initial conditions at the start of the model run at 2 Ma were set using past sea level data from[78], sedimentation rates from ref. [29], an assumed bottom water temperature of −1 °C, a linear thermal gradient of 65 °C km^{-1} [27]and a thermal diffusivity of 4.58×10^{-7} m^2 s^{-1} (based on thermal conductivity, specific heat capacity, and bulk density of sediments from ODP 912). The bottom water temperature is assumed to be constant throughout the model run. The water depth at the top boundary of the model varies over the period from 2 to 0.7 Ma based on the sea level and sedimentation rates. In contrast, the bottom boundary shifts along with changes in water depth, keeping the cell number constant. The diffusive heat transport resulting from sedimentation is estimated using an explicit finite-difference numerical solution of the heat equation[88,89] discounting heat flow variations due to hydrate formation and dissociation. The time step for the model run is estimated as 1/(4 × thermal diffusivity). The base of hydrate stability at each time step is then calculated by integrating the subsurface thermal profile with the theoretically predicted gas hydrate phase boundary generated using the CSMHYD programme[90]. This programme estimates the pressure at which hydrates are stable for any given temperature, taking into account the composition of gas-forming hydrates and the presence of inhibitors of hydrate formation (e.g., salt). We assume pure methane gas and a pore-water salinity of 35‰ for evaluating the hydrate phase boundary. The pressure estimate from CSMHYD is converted to depth using standard values for the density of seawater (1027 kg m^{-3}) and acceleration due to gravity (9.8 m s^{-2}), assuming hydrostatic pressure.

Data availability

The data used in this study can be accessed at https://doi.org/10.18710/FSLZAB, DataverseNO, V1.

Received: 8 August 2022; Accepted: 24 March 2023;
Published online: 08 April 2023

References

1. Ruppel, C. D. & Kessler, J. D. The interaction of climate change and methane hydrates. *Rev. Geophys.* **55**, 126–168 (2017).
2. Clark, P. U. et al. The middle Pleistocene transition: characteristics, mechanisms, and implications for long-term changes in atmospheric pCO2. *Quat. Sci. Rev.* **25**, 3150–3184 (2006).
3. Raymo, M. E. & Nisancioglu, K. H. The 41 kyr world: Milankovitch's other unsolved mystery. *Paleoceanography* **18**, https://doi.org/10.1029/2002PA000791 (2003).
4. Bajo, P. et al. Persistent influence of obliquity on ice age terminations since the Middle Pleistocene transition. *Science* **367**, 1235–1239 (2020).
5. Pena, L. D. & Goldstein, S. L. Thermohaline circulation crisis and impacts during the mid-Pleistocene transition. *Science* **345**, 318–322 (2014).
6. Detlef, H. et al. Sea ice dynamics across the Mid-Pleistocene transition in the Bering Sea. *Nat. Commun.* **9**, 941 (2018).
7. Elderfield, H. et al. Evolution of ocean temperature and ice volume through the mid-Pleistocene climate transition. *Science* **337**, 704 (2012).
8. Hönisch, B., Hemming, N. G., Archer, D., Siddall, M. & McManus, J. F. Atmospheric carbon dioxide concentration across the mid-Pleistocene transition. *Science* **324**, 1551–1554 (2009).
9. Clark, P. U. & Pollard, D. Origin of the middle Pleistocene transition by ice sheet erosion of regolith. *Paleoceanography* **13**, 1–9 (1998).
10. Knies, J. et al. The Plio-Pleistocene glaciation of the Barents Sea–Svalbard region: a new model based on revised chronostratigraphy. *Quat. Sci. Rev.* **28**, 812–829 (2009).
11. Berger, W. & Jansen, E. The polar oceans and their role in shaping the global environment. In *The Polar Oceans and Their Role in Shaping the Global Environment* Vol. 85, 295–311 (1994).
12. Andreassen, K., Ødegaard, C. M. & Rafaelsen, B. Imprints of former ice streams, imaged and interpreted using industry three-dimensional seismic data from the south-western Barents Sea. *Geol. Soc. Spe. Publ.* **277**, 151 (2007).
13. Laberg, J. S., Andreassen, K., Knies, J., Vorren, T. O. & Winsborrow, M. Late Pliocene–Pleistocene development of the Barents Sea Ice Sheet. *Geology* **38**, 107–110 (2010).
14. Flower, B. P. Overconsolidated section on the Yermak Plateau, Arctic Ocean: Ice sheet grounding prior to ca. 660 ka? *Geology* **25**, 147–150 (1997).
15. Kristoffersen, Y. et al. Seabed erosion on the Lomonosov Ridge, central Arctic Ocean: A tale of deep draft icebergs in the Eurasia Basin and the influence of Atlantic water inflow on iceberg motion? *Paleoceanography* **19**, https://doi.org/10.1029/2003PA000985 (2004).
16. Knies, J. et al. Effects of Arctic freshwater forcing on thermohaline circulation during the Pleistocene. *Geology* **35**, 1075 (2007).
17. Farmer, J. R. et al. Deep Atlantic Ocean carbon storage and the rise of 100,000-year glacial cycles. *Nat. Geosci.* **12**, 355–360 (2019).
18. MacLeod, M. K. Gas hydrates in ocean bottom sediments1. *AAPG Bulletin* **66**, 2649–2662 (1982).
19. Bohrmann, G. & Torres, M. E. In *Encyclopedia of Marine Geosciences* (eds Harff, J., Meschede, M., Petersen, S. & Thiede, J.) 1–7 (Springer Netherlands, 2013).
20. Andreassen, K. et al. Massive blow-out craters formed by hydrate-controlled methane expulsion from the Arctic seafloor. *Science* **356**, 948–953 (2017).
21. Serov, P. et al. Postglacial response of Arctic Ocean gas hydrates to climatic amelioration. *Proc. Natl Acad. Sci. USA.* **114**, 6215–6220 (2017).
22. Cremiere, A. et al. Timescales of methane seepage on the Norwegian margin following collapse of the Scandinavian Ice Sheet. *Nat. Commun.* **7**, 1–10 (2016).
23. Himmler, T. et al. A 160,000-year-old history of tectonically controlled methane seepage in the Arctic. *Sci. Adv.* **5**, 1–8 (2019).
24. Dessandier, P.-A. et al. Ice-sheet melt drove methane emissions in the Arctic during the last two interglacials. *Geology* **49**, 5 (2021).
25. Fischer, H. et al. Where to find 1.5 million yr old ice for the IPICS "Oldest-Ice" ice core. *Clim. Past* **9**, 2489–2505 (2013).
26. Daszinnies, M. et al. The Plio-Pleistocene seepage history off western Svalbard inferred from 3D petroleum systems modelling. *Mar. Pet. Geol.* **128**, 105023 (2021).
27. Myhre, A., Thiede, J. & Firth, J. In *Initial Reports* (College Station, TX, 1995).
28. Corliss, B. H. & Chen, C. Morphotype patterns of Norwegian Sea deep-sea benthic foraminifera and ecological implications. *Geology* **16**, 716–719 (1988).
29. Mattingsdal, R. et al. A new 6 Myr stratigraphic framework for the Atlantic–Arctic Gateway. *Quat. Sci. Rev.* **92**, 170–178 (2014).
30. Lisiecki, L. E. & Raymo, M. E. A Pliocene-Pleistocene stack of 57 globally distributed benthic δ18O records. *Paleoceanography* **20**, PA1003 (2005).
31. Shipley, T. H. et al. Seismic evidence for widespread possible gas hydrate horizons on continental slopes and rises. *AAPG Bulletin* **63**, 2204–2213 (1979).
32. Panieri, G. et al. Diagenetic Mg-calcite overgrowths on foraminiferal tests in the vicinity of methane seeps. *Earth Planet. Sci. Lett.* **458**, 203–212 (2016).

33. Wollenburg, J. E., Kuhnt, W. & Mackensen, A. Changes in Arctic Ocean paleoproductivity and hydrography during the last 145 kyr: the benthic foraminiferal record. *Paleoceanography* **16**, 65–77 (2001).
34. Schneider, A. et al. Methane seepage at Vestnesa Ridge (NW Svalbard) since the Last Glacial Maximum. *Quat. Sci. Rev.* **193**, 98–117 (2018).
35. Knudsen, K. L. & Seidenkrantz, M.-S. Stainforthia feylingi new species from arctic to subarctic environments, previously recorded as Stainforthia schreibersiana (Czjzek). *Cushman Found. Foraminifer. Res. Spe. Publ.* **32**, 5–13 (1994).
36. Niemann, H. & Elvert, M. Diagnostic lipid biomarker and stable carbon isotope signatures of microbial communities mediating the anaerobic oxidation of methane with sulphate. *Org. Geochem.* **39**, 1668–1677 (2008).
37. Jørgensen, B. B. Mineralization of organic matter in the sea bed—the role of sulphate reduction. *Nature* **296**, 643–645 (1982).
38. Knies, J. et al. Modelling persistent methane seepage offshore western Svalbard since early Pleistocene. *Mar. Pet. Geol.* **91**, 800–811 (2018).
39. Dickens, G. R., Castillo, M. M. & Walker, J. C. G. A blast of gas in the latest Paleocene: simulating first-order effects of massive dissociation of oceanic methane hydrate. *Geology* **25**, 259–262 (1997).
40. Kennett, J. P., Cannariato, K. G., Hendy, I. L. & Behl, R. J. Carbon isotopic evidence for methane hydrate instability during quaternary interstadials. *Science* **288**, 128 (2000).
41. Thomas, D. J., Zachos, J. C., Bralower, T. J., Thomas, E. & Bohaty, S. Warming the fuel for the fire: evidence for the thermal dissociation of methane hydrate during the Paleocene-Eocene thermal maximum. *Geology* **30**, 1067–1070 (2002).
42. Tripati, A. & Elderfield, H. Deep-sea temperature and circulation changes at the paleocene-eocene thermal maximum. *Science* **308**, 1894 (2005).
43. Rathburn, A. E. et al. Relationships between the distribution and stable isotopic composition of living benthic foraminifera and cold methane seep biogeochemistry in Monterey Bay, California. *Geochem. Geophys. Geosystems* **4**, https://doi.org/10.1029/2003GC000595 (2003).
44. Panieri, G. Foraminiferal response to an active methane seep environment: a case study from the Adriatic Sea. *Mar. Micropaleontol.* **61**, 116–130 (2006).
45. Bernhard, J. M. & Panieri, G. Keystone Arctic paleoceanographic proxy association with putative methanotrophic bacteria. *Sci. Rep.* **8**, 10610 (2018).
46. Claypool, G. E. & Kaplan, I. R. In *Natural Gases in Marine Sediments* 99–139 (Springer, 1974).
47. Fry, B. & Sherr, E. B. In *Stable Isotopes in Ecological Research* 196–229 (Springer New York, 1989).
48. Chuang, P.-C. et al. Carbon isotope exchange during anaerobic oxidation of methane (AOM) in sediments of the northeastern South China Sea. *Geochim. Cosmochim. Acta* **246**, 138–155 (2019).
49. Jennings, A. E., Hald, M., Smith, M. & Andrews, J. T. Freshwater forcing from the Greenland Ice Sheet during the Younger Dryas: evidence from southeastern Greenland shelf cores. *Quat. Sci. Rev.* **25**, 282–298 (2006).
50. Wollenburg, J. E., Knies, J. & Mackensen, A. High-resolution paleoproductivity fluctuations during the past 24 kyr as indicated by benthic foraminifera in the marginal Arctic Ocean. *Palaeogeogr. Palaeoclimatol. Palaeoecol.* **204**, 209–238 (2004).
51. Alve, E. Opportunistic features of the foraminifer Stainforthia fusiformis (Williamson): evidence from Frierfjord, Norway. *J. Micropalaeontol.* **13**, 24–24 (1994).
52. McCorkle, D. C., Keigwin, L. D., Corliss, B. H. & Emerson, S. R. The influence of microhabitats on the carbon isotopic composition of deep-sea benthic foraminifera. *Paleoceanography* **5**, 161 (1990).
53. Rathburn, A., Corliss, B., Tappa, K. & Lohmann, K. Comparisons of the ecology and stable isotopic compositions of living (stained) benthic foraminifera from the Sulu and South China Seas. *Deep Sea Res. Pt. I* **43**, 1617–1646 (1996).
54. Ambrose, W. et al. Bivalve shell horizons in seafloor pockmarks of the last glacial-interglacial transition: a thousand years of methane emissions in the Arctic Ocean. *Geochem. Geophys. Geosystem* **16**, 4108–4129 (2015).
55. Panieri, G. et al. An integrated view of the methane system in the pockmarks at Vestnesa Ridge, 79°N. *Mar. Geol.* **390**, 282–300 (2017).
56. Boetius, A. et al. A marine microbial consortium apparently mediating anaerobic oxidation of methane. *Nature* **407**, 623–626 (2000).
57. Knittel, K., Lösekann, T., Boetius, A., Kort, R. & Amann, R. Diversity and distribution of methanotrophic archaea at cold seeps. *Appl. Environ. Microbiol.* **71**, 467–479 (2005).
58. Knittel, K. & Boetius, A. Anaerobic oxidation of methane: progress with an unknown process. *Annu. Rev. Microbiol.* **63**, 311–334 (2009).
59. Yu, H. et al. Sulfate differentially stimulates but is not respired by diverse anaerobic methanotrophic archaea. *ISME J.* **16**, 168–177 (2022).
60. Milucka, J. et al. Zero-valent sulphur is a key intermediate in marine methane oxidation. *Nature* **491**, 541–546 (2012).
61. Elvert, M., Suess, E. & Whiticar, M. J. Anaerobic methane oxidation associated with marine gas hydrates: superlight C-isotopes from saturated and unsaturated C20 and C25 irregular isoprenoids. *Naturwissenschaften* **86**, 295–300 (1999).
62. Hinrichs, K.-U., Hayes, J. M., Sylva, S. P., Brewer, P. G. & DeLong, E. F. Methane-consuming archaebacteria in marine sediments. *Nature* **398**, 802–805 (1999).
63. Orphan, V. J., House, C. H., Hinrichs, K.-U., McKeegan, K. D. & DeLong, E. F. Methane-consuming archaea revealed by directly coupled isotopic and phylogenetic analysis. *Science* **293**, 484–487 (2001).
64. Niemann, H. et al. Novel microbial communities of the Haakon Mosby mud volcano and their role as a methane sink. *Nature* **443**, 854–858 (2006).
65. Lösekann, T. et al. Diversity and abundance of aerobic and anaerobic methane oxidizers at the Haakon Mosby Mud Volcano, Barents Sea. *Appl. Environ. Microbiol.* **73**, 3348–3362 (2007).
66. Blumenberg, M., Seifert, R., Reitner, J., Pape, T. & Michaelis, W. Membrane lipid patterns typify distinct anaerobic methanotrophic consortia. *Proc. Natl Acad. Sci. USA* **101**, 11111 (2004).
67. Aquilina, A. et al. Biomarker indicators for anaerobic oxidizers of methane in brackish-marine sediments with diffusive methane fluxes. *Org. Geochem.* **41**, 414–426 (2010).
68. Elvert, M., Boetius, A., Knittel, K. & Jørgensen, B. B. Characterization of specific membrane fatty acids as chemotaxonomic markers for sulfate-reducing bacteria involved in anaerobic oxidation of methane. *Geomicrobiol. J.* **20**, 403–419 (2003).
69. Plaza-Faverola, A. et al. Role of tectonic stress in seepage evolution along the gas hydrate-charged Vestnesa Ridge, Fram Strait. *Geophys. Res. Lett.* **42**, 733–742 (2015).
70. Chand, S. et al. Multiple episodes of fluid flow in the SW Barents Sea (Loppa High) evidenced by gas flares, pockmarks and gas hydrate accumulation. *Earth Planet. Sci. Lett.* **331-332**, 305–314 (2012).
71. Portnov, A. D., Vadakkepuliyambatta, S., Mienert, J. & Hubbard, A. L. Ice-sheet-driven methane storage and release in the Arctic. *Nat. Commun.* **7**, 1–7 (2016).
72. Moskvitch, K. Mysterious Siberian crater attributed to methane. *Nature* https://doi.org/10.1038/nature.2014.15649 (2014).
73. Bogoyavlensky, V. et al. New catastrophic gas blowout and giant crater on the Yamal Peninsula in 2020: results of the expedition and data processing. *Geosciences* **11**, 71 (2021).
74. Karstens, J. et al. Glacigenic sedimentation pulses triggered post-glacial gas hydrate dissociation. *Nat. Commun.* **9**, 635 (2018).
75. Sibson, R. H. Rupture nucleation on unfavorably oriented faults. *Bull. Seismol. Soc. Am.* **80**, 1580–1604 (1990).
76. Terakawa, T. et al. Effects of pore fluid pressure and tectonic stress on diverse seismic activities around the Mt. Ontake volcano, central Japan. *Tectonophysics* **608**, 138–148 (2013).
77. Plaza-Faverola, A. & Keiding, M. Correlation between tectonic stress regimes and methane seepage on the western Svalbard margin. *Solid Earth* **10**, 79–94 (2019).
78. Miller, K. G. et al. The phanerozoic record of global sea-level change. *Science* **310**, 1293 (2005).
79. Fjeldskaar, W. The amplitude and decay of glacial forebulge in Fennoscandia. *Norsk Geologisk Tidsskrift* **74**, 2–8 (1994).
80. Lien, Ø. F., Hjelstuen, B. O., Zhang, X. & Sejrup, H. P. Late Plio-Pleistocene evolution of the Eurasian Ice Sheets inferred from sediment input along the northeastern Atlantic continental margin. *Quat. Sci. Rev.* **282**, 107433 (2022).
81. Gautier, D. L. et al. Assessment of undiscovered oil and gas in the Arctic. *Science* **324**, 1175–1179 (2009).
82. Mau, S. et al. Widespread methane seepage along the continental margin off Svalbard-from Bjørnøya to Kongsfjorden. *Sci. Rep.* **7**, 1–13 (2017).
83. Skarke, A., Ruppel, C., Kodis, M., Brothers, D. & Lobecker, E. Widespread methane leakage from the sea floor on the northern US Atlantic margin. *Nat. Geosci.* **7**, 657–661 (2014).
84. Dyonisius, M. N. et al. Old carbon reservoirs were not important in the deglacial methane budget. *Science* **367**, 907–910 (2020).
85. Wollenburg, J. E. & Mackensen, A. Living benthic foraminifers from the central Arctic Ocean: faunal composition, standing stock and diversity. *Mar. Micropaleontol.* **34**, 153–185 (1998).
86. Consolaro, C. et al. Carbon isotope (δ13C) excursions suggest times of major methane release during the last 14 kyr in Fram Strait, the deep-water gateway to the Arctic. *Clim. Past* **11**, 669–685 (2015).
87. Panieri, G. et al. Record of methane emissions from the West Svalbard continental margin during the last 23.500 yrs revealed by δ13C of benthic foraminifera. *Glob. Planet. Change* **122**, 151–160 (2014).
88. Gerya, T. *Introduction to Numerical Geodynamic Modelling* (Cambridge University Press, 2019).
89. Phrampus, B. J. & Hornbach, M. J. Recent changes to the Gulf Stream causing widespread gas hydrate destabilization. *Nature* **490**, 527–530 (2012).
90. Sloan Jr, E. D. & Koh, C. A. *Clathrate Hydrates of Natural Gases* (CRC Press, 2007).

91. Svendsen, J. I. et al. Late Quaternary ice sheet history of northern Eurasia. *Quat. Sci. Rev.* **23**, 1229–1271 (2004).
92. Gebhardt, A. et al. Ice sheet grounding and iceberg plow marks on the northern and central Yermak Plateau revealed by geophysical data. *Quat. Sci. Rev.* **30**, 1726–1738 (2011).
93. Lourens, L., Hilgen, F., Shackleton, N. J., Laskar, J. & Wilson, D. In *A Geologic Time Scale 2004* (eds Smith, A. G., Gradstein, F. M. & Ogg, J. G.) 409–440 (Cambridge University Press, 2005).
94. Schneider, A., Cremiere, A., Panieri, G., Lepland, A. & Knies, J. Diagenetic alteration of benthic foraminifera from a methane seep site on Vestnesa Ridge (NW Svalbard). *Deep Sea Res. Pt. I* **123**, 22–34 (2017).

Acknowledgements

We sincerely thank the staff at the IODP core repository in Bremen, Germany, for all their help during various sampling parties. The research was supported by the Norwegian Research Council (project numbers 223259, 255150, and 287869). We thank Karin Andreassen for providing the seismic profile from the Yermak Plateau, Patrycja Jernas for the support in the foraminifera investigation, Torger Grytå for the artwork, Fredrik Sahlström for help with the SEM observations, the NGU laboratory staff for the sulfur analyses, Serge Robert for biomarker analyses. We also thank Barun Sen Gupta and Claudio Argentino for helpful discussion, and Eawag for funding Carsten J. Schubert.

Author contributions

G.P., J.K., and S.V. developed the main idea. G.P., J.K., and S.V. wrote the first version of the manuscript. The age model was done by J.K. The biomarker analyses and interpretation were performed by C.J.S., and the micropaleontological work was performed by G.P. Sulfur analyses were performed by J.K., and A.L.L. assisted with the energy-dispersive X-ray spectroscopy (EDS) and electron backscattered diffraction (EBSD) analyses. S.V. performed geophysical data interpretation and modelling. All authors discussed the results and commented on the manuscript.

Funding

Open access funding provided by UiT The Arctic University of Norway (incl University Hospital of North Norway).

Competing interests

The authors declare no competing interests.

Additional information

Supplementary information The online version contains supplementary material available at https://doi.org/10.1038/s43247-023-00772-y.

Correspondence and requests for materials should be addressed to Giuliana Panieri.

Peer review information *Communications Earth & Environment* thanks Daidai Wu and the other, anonymous, reviewer(s) for their contribution to the peer review of this work. Primary Handling Editors: Clare Davis.

Reprints and permission information is available at http://www.nature.com/reprints

Publisher's note Springer Nature remains neutral with regard to jurisdictional claims in published maps and institutional affiliations.

Open Access This article is licensed under a Creative Commons Attribution 4.0 International License, which permits use, sharing, adaptation, distribution and reproduction in any medium or format, as long as you give appropriate credit to the original author(s) and the source, provide a link to the Creative Commons license, and indicate if changes were made. The images or other third party material in this article are included in the article's Creative Commons license, unless indicated otherwise in a credit line to the material. If material is not included in the article's Creative Commons license and your intended use is not permitted by statutory regulation or exceeds the permitted use, you will need to obtain permission directly from the copyright holder. To view a copy of this license, visit http://creativecommons.org/licenses/by/4.0/.

© The Author(s) 2023